Magnesium Technology 2013
Edited by: Norbert Hort, Suveen N. Mathaudhu, Neale R. Neelameggham, and Martyn Alderman
TMS (The Minerals, Metals & Materials Society), 2013

NANOPARTICLE ADDITION TO ENHANCE THE MECHANICAL RESPONSE OF MAGNESIUM ALLOYS INCLUDING NANOSCALE DEFORMATION MECHANISMS

Muralidharan Paramsothy*, Manoj Gupta
Department of Mechanical Engineering, National University of Singapore
9 Engineering Drive 1, Singapore 117576

Keywords: Nanoparticles, Magnesium alloys, Mechanical properties, NENID, Nanoscale deformation mechanisms.

Abstract

In this study, various magnesium alloy nanocomposites derived from AZ (Aluminium-Zinc) or ZK (Zinc-Zirconium) series matrices and containing Al_2O_3, Si_3N_4, TiC or carbon nanotube (CNT) nanoparticle reinforcement (representative oxide, nitride, carbide or carbon nanoparticle reinforcement, respectively) were fabricated using solidification processing followed by hot extrusion. The main aim here was to simultaneously enhance tensile strength and ductility of each alloy using nanoparticles. The magnesium-oxygen strong affinity and magnesium-carbon weak affinity (comparison of extremes in affinity) are both well known in the context of magnesium composite processing. However, an approach to possibly quantify this affinity in magnesium nanocomposite processing is not clear. In this study accordingly, Nanoscale Electro Negative Interface Density or NENID quantifies the nanoparticle-alloy matrix interfacial area per unit volume in the magnesium alloy nanocomposite taking into consideration the electronegativity of the nanoparticle reinforcement. The beneficial (as well as comparative) effect of the nanoparticles on each alloy is discussed in this article. Regarding the mechanical performance of the nanocomposites, it is important to understand the experimentally observed nanoparticle-matrix interactions during plastic deformation (nanoscale deformation mechanisms). Little is known in this area based on direct observations for metal matrix nanocomposites. Here, relevant multiple nanoscale phenomena includes the emanation of high strain zones (HSZs) from nanoparticle surfaces.

Introduction

In comparing nanocomposites to microcomposites, the particle reinforcement is at nanoscale where physically confined yet beneficial effects are imparted to the host matrix. The function of nanoparticles in a metallic matrix is related to: (a) nanoparticle-matrix reactivity and (b) nanoparticle distribution in the matrix. Both factors can strongly affect the mechanical (crystallographic structure related) or functional (electronic structure related) properties of the composite. Magnesium alloys are an easily available lightweight and energy saving metallic matrix. The AZ (Aluminium-Zinc) series of magnesium alloys are characterized by: (a) low cost, (b) ease of handling, (c) good strength and ductility and (d) resistance to atmospheric corrosion [1]. The ZK (Zinc-Zirconium) series of magnesium alloys are characterized by: (a) high strength and ductility after T5 aging, (b) good creep resistance, (c) poor arc weldability due to hot-shortness cracking and (d) excellent resistance weldability. These qualities enable the common use of AZ and ZK series magnesium alloys [1]. Regarding metal matrix nanocomposites as abundant interface area systems, the ways to reduce chemical reactivity at the nanoparticle-metal matrix interface during solidification processing are extremely limited. It is necessary to take into consideration the: (1) Pauling electronegativity of the nanoparticle (El_{np}) and (2) electronegativity difference between the nanoparticle and the alloy matrix ($El_{np} - El_{alloy}$) to understand the chemical reactivity at the nanoparticle-alloy matrix interface. Electron attraction leading to chemical reaction increases with El_{np} while chemical reactivity at the nanoparticle-alloy matrix interface also increases with ($El_{np} - El_{alloy}$). Much of the existing representative research literature on solidification processed magnesium alloy nanocomposites indicates that: (a) good nanoparticle distribution can be achieved in the magnesium matrix and (b) better mechanical properties can be achieved due to the addition of nanoparticles [2-6]. However, it is important to understand the experimentally observed nanoparticle-matrix interactions during plastic deformation regarding the mechanical performance of a nanocomposite. Considering metal matrix nanocomposites, little is known in this area based on direct observations. The interaction between carbon nanotubes (CNTs) and aluminium based matrix during deformation has been briefly documented [7-9]. Here, the aluminium/CNT nanocomposites were deformed to 2% and transmission electron microscopy (TEM) revealed regions of severe deformation (based on high electron contrast) near the CNT tips in the aluminium based matrix. Dislocation accumulation at the aluminium/CNT interface was also observed in the 2% deformed nanocomposites. Comparatively, there are more reports based on modelling and simulation as compared to direct experimental observations regarding deformation mechanisms in metal matrix nanocomposites [10, 11].

Accordingly, this study is aimed at understanding the beneficial (as well as comparative) effect of representative oxide, nitride, carbide and carbon nanotube (CNT) nanoparticles on AZ and/or ZK series magnesium alloys taking Nanoscale Electro Negative Interface Density or NENID as well as the experimentally observed nanoparticle-matrix interactions during physical deformation into consideration. NENID quantifies the nanoparticle-alloy matrix affinity based on interfacial area per unit volume in the alloy nanocomposite taking into consideration the electronegativity of the nanoparticle reinforcement. Disintegrated melt deposition (DMD) [12] followed by hot extrusion was used to synthesize the magnesium alloy nanocomposites.

Experimental Procedures

The materials used in this study are listed in Table I. The matrix materials used were: (1) AZ31, (2) AA5083 for metallurgically upgrading AZ31 (addition of 3 wt.% relative to AZ31 weight), (3) AZ61, (4) AA1050 for metallurgically upgrading AZ61 (addition of 2 wt.% relative to AZ31 weight), (5) AZ91 for metallurgically upgrading AZ31 (nominal Al content of AZ31 increased by 3 wt.%.) and (6) ZK60A. All alloy pieces were sectioned to smaller pieces. All oxide and scale surfaces were removed using machining. All surfaces were washed with ethanol after machining. Reinforcement materials used were: (1) Al_2O_3

Table I. Materials selected for this study

Material	Available description and/or composition (wt%)	Particle size (nm)	Source
Alloys			
AZ31	nominally 2.40-3.60 wt.% Al, 0.50-1.50 wt.% Zn, 0.15-1.00 wt.% Mn, 0.10 wt.% Si max, 0.10 wt.% Cu max, 0.03 wt.% Ni max, 0.30.wt% others max, balance Mg	-	Alfa Aesar, Massachusetts, USA
AA5083	nominally 4.0-4.9 wt.% Mg, 0.40 wt.% Si, 0.40 wt.% Fe, 0.10 wt.% Cu, 0.40-1.00 wt.% Mn, 0.05-0.25 wt.% Cr, 0.25 wt.% Zn, 0.15 wt.% Ti, 0.15 wt.% others, balance Al	-	Yan San Metals Pte. Ltd., Singapore
AZ61	nominally 5.8-7.2 wt.% Al, 0.15-0.50 wt.% Mn, 0.04-1.50 wt.% Zn, 0.10 wt.% Si max, 0.05 wt.% Cu max, 0.005 wt.% Ni max, 0.005 wt.% Fe max, 0.30 wt.% others max, balance Mg	-	Tokyo Magnesium Co. Ltd., Yokohama, Japan
AA1050	nominally > 99.5 wt.% Al	-	Alfa Aesar, Massachusetts, USA
AZ91	nominally 8.30-9.70 wt.% Al, 0.35-1.00 wt.% Zn, 0.15-0.50 wt.% Mn, 0.10 wt.% Si, 0.030 wt.% Cu, 0.005 wt.% Fe, 0.002 wt.% Ni, 0.02 wt.% others, balance Mg	-	Tokyo Magnesium Co. Ltd., Yokohama, Japan
ZK60A	nominally 4.80-6.20 wt.% Zn, 0.45 wt.% Zr min, 0.30 wt.% others max, balance Mg	-	Tokyo Magnesium Co. Ltd., Yokohama, Japan
Nanoparticles			
Al_2O_3	γ-alumina	30-70	Baikowski, Japan
CNT	vapor grown, 94.7 % purity, up to 100 aspect ratio (Al-Saleh and Sundararaj 2009)	40-70	Nanostructured & Amorphous Materials Inc, Texas, USA
TiC	98+ % purity	30-50	Nanostructured & Amorphous Materials Inc, Texas, USA
Si_3N_4	98.5+ % purity	15-30	Nanostructured & Amorphous Materials Inc, Texas, USA

Please note that AZ31, AZ61, AZ91 and ZK60A are magnesium alloys while AA5083 and AA1050 are aluminium alloys.

nanoparticles, (2) carbon nanotube (CNT) nanoparticles, (3) TiC nanoparticles and (4) Si_3N_4 nanoparticles. Monolithic AZ31, AZ31/AA5083 (nominal Al content of AZ31 increased by 3 wt.%), AZ31/AZ91 hybrid alloy (nominal Al content of AZ31 increased by 3 wt.%), AZ81 (nominal Al content of AZ61 increased by 2 wt.% using AA1050) and ZK60A were each cast using the DMD method [12, 13]. This involved heating all alloy pieces to 750°C in an inert Ar gas atmosphere in a graphite crucible using a resistance heating furnace. The crucible was equipped with an arrangement for bottom pouring. Upon reaching the superheat temperature, the molten slurry was stirred for 2.5min at 460rpm using a twin blade (pitch 45°) mild steel impeller to facilitate the uniform distribution of heat. The impeller was coated with Zirtex 25 (86%ZrO_2, 8.8%Y_2O_3, 3.6%SiO_2, 1.2%K_2O and Na_2O, and 0.3% trace inorganics) to avoid iron contamination of the molten metal. The melt was then released through a 10mm diameter orifice at the base of the crucible. The melt was disintegrated by two jets of argon gas oriented normal to the melt stream located 265mm from the melt pouring point. The argon gas flow rate was maintained at 25lpm. The disintegrated melt slurry was subsequently deposited onto a metallic substrate located 500mm from the disintegration point. An ingot of 40mm diameter was obtained following the deposition stage. To form the corresponding alloy nanocomposites (1.0-1.5 vol.% reinforcement content), Al_2O_3, Si_3N_4, TiC or CNT nanoparticle powder was isolated by wrapping in Al foil of minimal weight (< 0.50 wt.% with respect to the total matrix weight) and arranged on top of the alloy pieces, with all other DMD parameters unchanged. All billets were machined to 35mm diameter and hot extruded using 20.25:1 extrusion ratio on a 150 ton hydraulic press. The extrusion temperature was 350 °C. The billets were held at 400 °C for 60 min in a furnace prior to extrusion. Colloidal graphite was used as a lubricant. Rods of 8 mm were obtained.

Prior to tensile or compressive deformation, microstructural characterization studies were conducted on metallographically polished monolithic and nanocomposite extruded samples to determine grain characteristics. Hitachi S4300 Field-Emission SEM was used. Image analysis using Scion software was carried out to determine the grain characteristics. Thin foils were prepared from the nanocomposite extruded samples using disc punch-out and ion-milling for (regarding localized effects): (a) nanoparticle distribution as well as (b) nanoparticle-matrix reactivity observation (based on selected area electron diffraction (SAED)) using transmission electron microscopy (JEOL JEM 3010 TEM with 300keV accelerating voltage). Regarding SAED, nanopowder samples (reinforcement dispersed in ethanol) were also prepared by droplet application onto holey carbon film mounted on copper grids followed by drying. All k-space measurements (k) from SAED patterns were manually obtained and converted to crystallographic lattice d-spacings (d) based on $d = 2\pi / k$. Goniometer XRD studies were conducted using CuK_α radiation (λ = 1.5406 Å) with a scan speed of 2 °/min in an automated Shimadzu LAB-X XRD-6000 diffractometer to determine the intermetallic phase(s) present and dominant textures in the transverse and longitudinal (extrusion) directions (regarding globalised effects). All d-spacings from SAED and goniometer XRD analysis were matched with corresponding d-spacings in the JCPDS database available in the Shimadzu LAB-X XRD-6000 diffractometer operating software to determine all phases present.

Table II. Nanoparticle size, interfacial area and electronegativity characteristics

Nanoparticle	Average size (nm) [a]	Average interfacial area x 10^3, IA (cm^2/cc) [b]	Average electronegativity, E [c]	$E - E_{matrix}$ [d]	NENID x 10^3 (cm^2/cc) [e]
CNT(X)	55.0 (40-70)	7.3	2.55	1.22	19 (15-26)
CNT(Y)	55.0 (40-70)	10.9	2.55	1.22	28 (22-38)
Al_2O_3	50.0 (30-70)	18.0	2.71	1.38	49 (35-81)
TiC	40.0 (30-50)	22.5	2.05	0.72	46 (37-62)
Si_3N_4	22.5 (15-30)	40.0	2.55	1.22	102 (77-153)

[a] Brackets indicate the available size (diameter) range of each nanoparticle.

[b] Nanoparticle-matrix interfacial area per cc in 1.5vol% nanocomposite in all cases except CNT(X) which is for 1.0 vol% nanocomposites. Nanoparticles assumed to be spherical (except in the case of CNT) and uniformly distributed in the matrix.

[c] Electronegativities of Al, O, Ti, C, Si and N are 1.61, 3.44, 1.54, 2.55, 1.90 and 3.04, respectively. E is the atomic (stoichiometric) average.

[d] Electronegativities of Mg, Al, Zn and Zr are 1.31, 1.61, 1.65 and 1.33, respectively. E_{matrix} is the weighted average based on the alloy matrix composition. In the case of the AZ31, AZ31/AA5083, AZ31/AZ91, AZ81 and ZK60A matrix compositions, $1.32 < E_{matrix} < 1.34$. $E_{matrix} \sim 1.33$.

[e] Nanoscale Electro Negative Interface Density or NENID = IA x E. Brackets indicate the range of calculated values based on the available size (diameter) range of each nanoparticle.

After tensile or compressive deformation, thin foils were prepared from the deformed nanocomposite extruded samples using disc punch-out and ion-milling for (regarding localized effects) high strain zone (HSZ) observation using a JEOL JEM 3010 transmission electron microscope.

Smooth bar tensile properties of the monolithic and nanocomposite extruded samples were determined based on ASTM E8M-05. Round tension test samples of 5 mm diameter and 25 mm gauge length were subjected to tension using an MTS 810 machine equipped with an axial extensometer with a crosshead speed set at 0.254 mm/min. 6-9 specimens were tested per formulation.

Results and Discussion

Synthesis of monolithic alloys and corresponding nanocomposites

Synthesis of monolithic and nanocomposite materials, the final form being extruded rods, was successfully accomplished with: (a) no detectable metal oxidation and (b) no detectable reaction between graphite crucible and melts. The inert atmosphere used during DMD was effective in preventing oxidation of the Mg melt. No stable carbides of Mg formed due to reaction with the graphite crucible.

Effect of nanoparticle electronegativity on tensile behavior

Nanoparticle size, interfacial area and electronegativity characteristics are listed in Table II. E is the stoichiometric average electronegativity of the nanoparticle. E_{matrix} is the weighted average electronegativity of the alloy matrix. In this study, $E_{matrix} \sim 1.33$. The AZ (aluminium-zinc) and ZK (zinc-zirconium) series of magnesium alloys are major representations of mainly aluminium containing and mainly zinc containing magnesium alloys (respectively) which collectively cover a significant portion of the entire range of solidification processed commercial magnesium alloys. $(E - E_{matrix})$ is the difference in electronegativity between the nanoparticle and alloy matrix. Nanoscale Electro Negative Interface Density or NENID is the product of IA (nanoparticle-matrix interfacial area per unit volume) and E. The range of calculated values of NENID is based on the available size (diameter) range of each nanoparticle. The NENID ranges of the different chemical types of nanoparticles listed (in brackets) in Table II were of an overlapping nature. The intention of this investigation was to provide as fair as possible representation to: (1) each chemical type of nanoparticle listed (oxide, nitride, carbide and pure carbon) and (2) the entire range of solidification processed commercial magnesium alloys as significantly covered by mainly aluminium containing and mainly zinc containing magnesium alloys.

The overall results of ambient temperature tensile testing of the extruded materials are shown in Table III. Among the tensile properties investigated, failure strain increment varied significantly with NENID as indicated by the simply fitted linear trend lines across the somewhat scattered data points for all plots in Figure 1 (increments are with respect to the corresponding mechanical property of the monolithic alloy). The scatter in data points was expected given the difference in chemical compositions among the various magnesium alloy matrices involved in this study. In the alloy nanocomposites, no nanoparticle-alloy matrix reaction products having more than 2% by volume were detected using X-ray diffraction analysis. Accordingly, it was expected that if nanoparticle-alloy matrix reaction products were formed, their size and volume fractions would be small, making detection by advanced methods difficult (or non-convincing at the least). Compared to the Al_2O_3, TiC and CNT nanocomposites (under non-equilibrium conditions), it was possible that the Si_3N_4 nanocomposites experienced more nanoparticle-alloy matrix interfacial reactions when: (1) NENID in the Si_3N_4 nanocomposites was up to 10 times that of the other nanocomposites (see Table II) and (2) $(E - E_{matrix})$ in the Si_3N_4 nanocomposite was sufficiently high at 1.22 (compared to 1.38 for the Al_2O_3 nanocomposites). This was the possible cause for the tensile failure strain increment of the Si_3N_4 nanocomposites to be

Table III. Results of tensile testing of magnesium alloys and related nanocomposites

Material	NENID x 10^3 (cm^2/cc)	0.2%TYS (MPa)	UTS (MPa)	Tensile failure strain (%)
AZ31	-	172 ± 15	263 ± 12	10.4 ± 3.9
AZ31/1.0vol%CNT	19	190 ± 13 (+10)	307 ± 10 (+17)	17.5 ± 2.6 (+68)
AZ31/1.5vol%Al_2O_3	49	204 ± 8 (+19)	317 ± 5 (+21)	22.2 ± 2.4 (+113)
AZ31/AA5083	-	203 ± 4	310 ± 4	8.7 ± 1.8
AZ31/AA5083/1.0vol%CNT	19	221 ± 4 (+9)	321 ± 1 (+4)	12.0 ± 1.0 (+38)
AZ31/AZ91	-	207 ± 4	316 ± 6	8.0 ± 0.1
AZ31/AZ91/1.5vol%Al_2O_3	49	232 ± 13 (+12)	339 ± 10 (+7)	15.9 ± 0.5 (+99)
AZ31/AZ91/1.5vol%TiC	46	236 ± 8 (+14)	337 ± 7 (+7)	14.5 ± 0.7 (+81)
AZ31/AZ91/1.5vol%Si_3N_4	102	232 ± 2 (+12)	331 ± 2 (+5)	13.1 ± 0.5 (+64)
AZ81	-	227 ± 3	321 ± 2	8.7 ± 0.9
AZ81/1.5vol%CNT	28	209 ± 9 (-8)	328 ± 4 (+2)	13.7 ± 2.2 (+57)
AZ81/1.5vol%Al_2O_3	49	212 ± 12 (-7)	339 ± 11 (+6)	13.1 ± 1.0 (+51)
AZ81/1.5vol%Si_3N_4	102	229 ± 9 (+1)	328 ± 7 (+2)	10.7 ± 0.9 (+23)
ZK60A	-	182 ± 4	271 ± 1	6.7 ± 1.0
ZK60A/1.0vol%CNT	19	180 ± 6 (-1)	295 ± 8 (+9)	15.0 ± 0.7 (+124)
ZK60A/1.5vol%TiC	46	184 ± 2 (+1)	309 ± 3 (+14)	11.6 ± 1.4 (+73)
ZK60A/1.5vol%Si_3N_4	102	198 ± 6 (+9)	313 ± 4 (+16)	12.2 ± 0.8 (+82)

( ) Brackets indicate % change with respect to corresponding result of monolithic alloy.

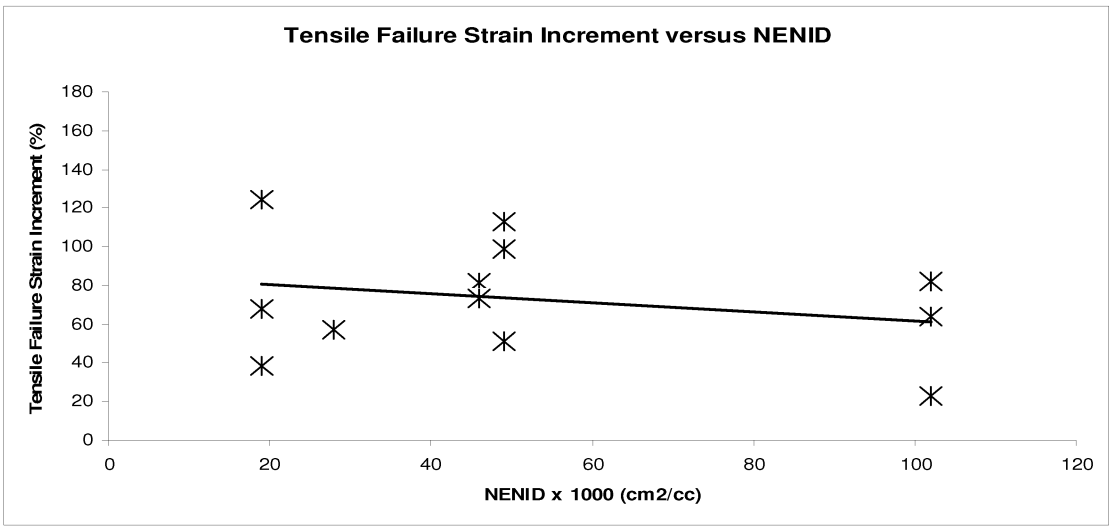

Figure 1. Significant variation of tensile failure strain increment with NENID as indicated by the simply fitted linear trend lines across the somewhat scattered data points for all plots. The scatter in data points was expected given the difference in chemical compositions among the various magnesium alloy matrices involved in this study. Please also note the overlapping NENID ranges of the different chemical types of nanoparticles listed (in brackets) in Table II.

closest to the bottom of the whole range exhibited by all the nanocomposites. Additionally, representative TEM SAED analysis for the Si_3N_4 nanocomposites is shown in Figure 2. Generally, TEM SAED occasionally indicated only for the Si_3N_4 nanocomposites that the Mg_3N_2 reaction product was formed. Also, the Si_3N_4 nanoparticle was originally amorphous in the as-supplied form but adopted a crystalline structure in the nanocomposite. In all other nanocomposites, no reaction product was *reliably* detected even by using TEM SAED. It was precisely for this reason (as previously mentioned) that it was expected that

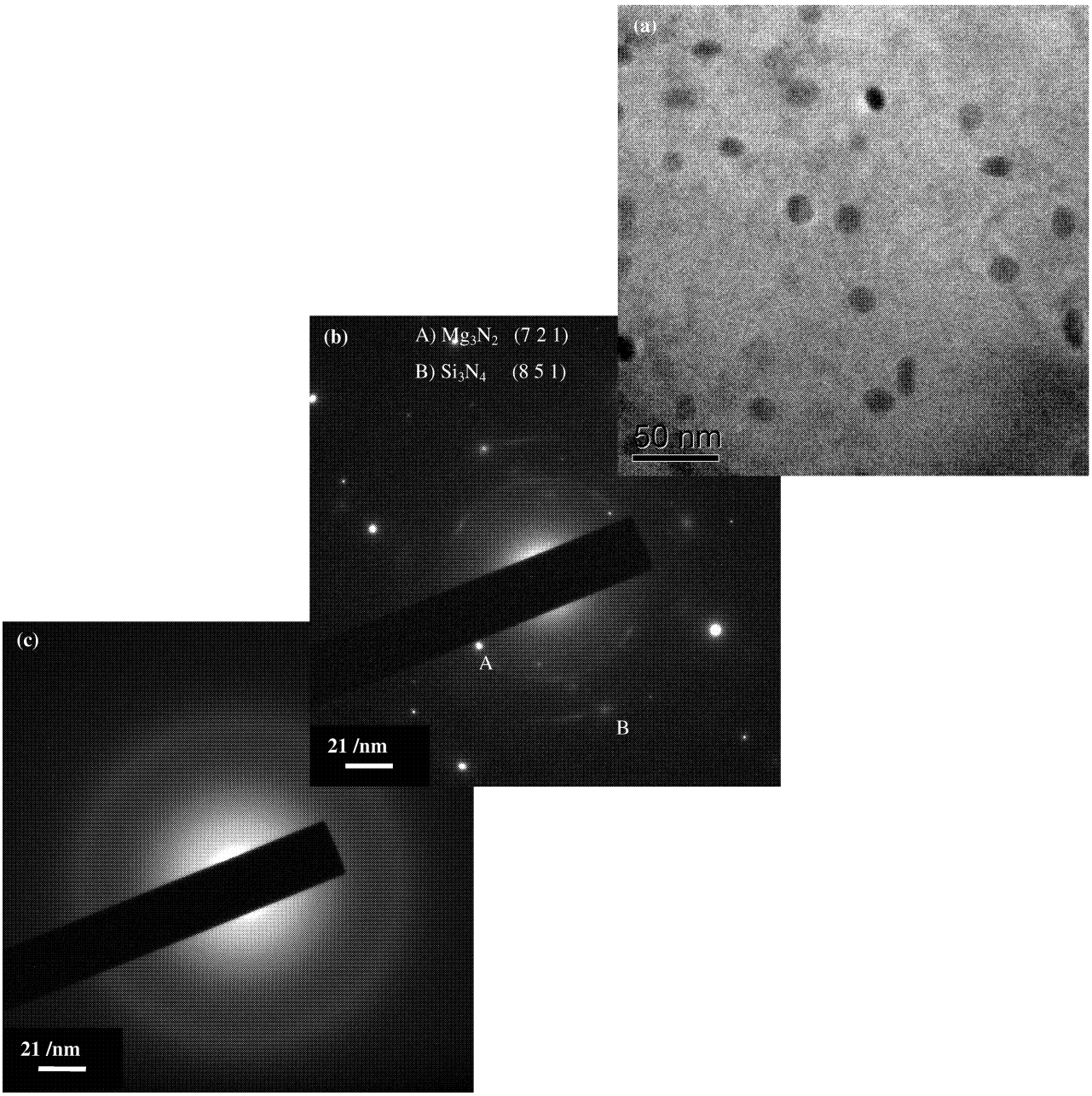

Figure 2. Representative TEM micrographs showing the: (a) presence of individual nanoparticles in each nanocomposite, (b) SAED pattern of Si_3N_4 nanocomposites and (c) SAED pattern of Si_3N_4 nanoparticles. Phases present but not labelled in the SAED pattern (in (b)) include Mg, Mg-Al and Mg-Zn phases only.

if nanoparticle-alloy matrix reaction products were formed, their size and volume fractions would be small, making detection by advanced methods difficult or non-convincing at the least.

Nanoscale Deformation Mechanisms

In each tensile deformed nanocomposite, the significant formation of high strain zones (HSZs) comprising dislocation slip was observed as shown in Figure 3. The uneven localizations of strain within the HSZ lead to: (a) severe electron contrast and (b) relatively less focus during TEM imaging. Figure 3a shows the emanation of the HSZ from a nanoparticle of approximately 100nm diameter. This direct observation of particle surface induced HSZ formation indicates the nanoscale dual role of fine particles in the magnesium matrix towards simultaneous strengthening and ductility enhancement. Strain hardening and dislocation slip within the HSZ contribute to strengthening and ductility enhancement, respectively. The HSZ formation from the particle surface also leads to shielding of the particle (and its immediate vicinity) from advancing nanoscale cracks, this being a tensile toughening mechanism. In the case of CNT nanocomposites, HSZs were formed to a significantly lower extent in the deformed nanocomposite compared to the near-spherical (and significantly lower aspect ratio) nanoparticle

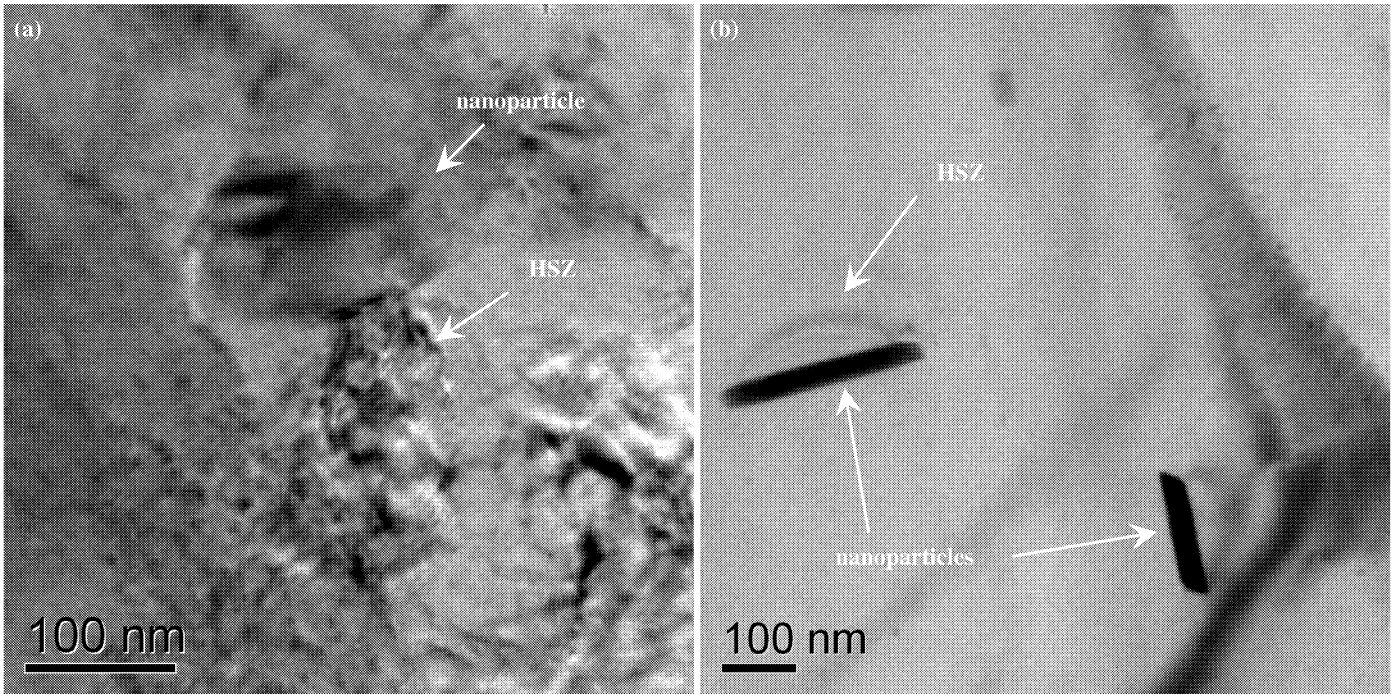

Figure 3. (a) Near-spherical nanoparticle induced HSZ formation and (b) higher aspect ratio nanoparticle induced relatively smaller bow-shaped HSZ formation in the deformed magnesium alloy matrix.

nanocomposite counterparts. Figure 3b shows the bow-shaped and relatively smaller HSZ formed around the CNT. This indicates the lower inclination of CNTs in the deformed magnesium matrix towards nanoscale ductility enhancement compared to nanoscale strength enhancement due to their increased aspect ratio at nanoscale.

Conclusions

1. The tensile failure strain increment of the Si_3N_4 nanocomposites were each closest to the bottom of the whole range exhibited by all the nanocomposites.
2. Compared to the Al_2O_3, TiC and CNT nanocomposites (under non-equilibrium conditions), it was possible that the Si_3N_4 nanocomposites experienced more nanoparticle-alloy matrix interfacial reactions when: (1) NENID in the Si_3N_4 nanocomposites was up to 10 times that of the other nanocomposites and (2) $(E - E_{matrix})$ in the Si_3N_4 nanocomposite was sufficiently high at 1.22 (compared to 1.38 for the Al_2O_3 nanocomposites).
3. The direct observation of particle surface induced HSZ formation indicates the nanoscale dual role of fine particles in the magnesium matrix towards simultaneous strengthening and ductility enhancement. Strain hardening and dislocation slip within the HSZ contribute to strengthening and ductility enhancement, respectively.
4. When the nanoparticle in the deformed magnesium alloy matrix has a higher aspect ratio (as in the case of CNT nanoparticles), it is less inclined towards nanoscale ductility enhancement compared to nanoscale strength enhancement.

References

[1] M.M. Avedesian, H. Baker, *ASM Specialty Handbook: Magnesium and Magnesium Alloys* (Ohio, OH: ASM International®, 1999) 12-25.

[2] M. Paramsothy, S.F. Hassan, N. Srikanth, M. Gupta, "Enhancing tensile/compressive response of magnesium alloy AZ31 by integrating with Al_2O_3 nanoparticles," *Mater. Sci. Eng. A*, 527 (2009), 162-168.

[3] M. Paramsothy, S.F. Hassan, N. Srikanth, M. Gupta, "Simultaneous enhancement of tensile/compressive strength and ductility of magnesium alloy AZ31 using carbon nanotubes," *J. Nanosci. Nanotechnol.*, 10 (2010), 956-964.

[4] M. Paramsothy, J. Chan, R. Kwok, M. Gupta, "Enhanced mechanical response of hybrid alloy AZ31 / AZ91 based on the addition of Si_3N_4 nanoparticles," *Mater. Sci. Eng. A*, 528 (2011), 6545-6551.

[5] M. Paramsothy, J. Chan, R. Kwok, M. Gupta, "TiC nanoparticle addition to enhance the mechanical response of hybrid magnesium alloy," *J. Nanotechnol.*, (2011), DOI: 10.1155/2011/401574.

[6] M. De Cicco, H. Konishi, G. Cao, H.S. Choi, L.S. Turng, J.H. Perepezko, S. Kou, R. Lakes, X. Li, "Strong, ductile magnesium zinc nanocomposites," *Metall. Mater. Trans. A*, 40 (2009), 3038-3045.

[7] H.J. Choi, J.H. Shin, B.H. Min, D.H. Bae, "Deformation behavior of Al–Si alloy based nanocomposites reinforced with carbon nanotubes," *Comp. Part A*, 41 (2010), 327-329.

[8] H.J. Choi, J.H. Shin, D.H. Bae, "Grain size effect on the strengthening behavior of aluminum-based composites containing multi-walled carbon nanotubes," *Comp. Sci. Technol.*, 71 (2011), 1699-1705.

[9] H.J. Choi, J.H. Shin, B.H. Min, J.S. Park, D.H. Bae, "Reinforcing effects of carbon nanotubes in structural aluminum matrix nanocomposites," *J. Mater. Res.*, 24(8) (2009), 2610-2616.

[10] H.T. Liu, L.Z. Sun, "Multi-scale modeling of elastoplastic deformation and strengthening mechanisms in aluminum-based amorphous nanocomposites," *Acta Mater.*, 53 (2005), 2693-2701.

[11] D.K. Ward, W.A. Curtin, Y. Qi, "Mechanical behavior of aluminum–silicon nanocomposites: A molecular dynamics study," *Acta Mater.*, 54 (2006), 4441-4451.

[12] L.M. Tham, M. Gupta, L. Cheng, "Influence of processing parameters during disintegrated melt deposition processing on near net shape synthesis of aluminium based metal matrix composites," *Mater. Sci. Technol.*, 15 (1999), 1139-1146.